Plasma Sources Sci. Technol. **10** (2001) 502–512 PII: S0963-0252(01)22553-5

Sources of azimuthal asymmetries in ionized metal physical vapour deposition processes

Junqing Lu[1,3] and Mark J Kushner[2,4]

[1] Department of Mechanical and Industrial Engineering, University of Illinois, 1406 W. Green Street, Urbana, IL 61801, USA
[2] Department of Electrical and Computer Engineering, University of Illinois, 1406 W. Green Street, Urbana, IL 61801, USA

E-mail: junqing.lu@novellus.com and mjk@uiuc.edu

Received 2 March 2001, in final form 31 May 2001
Published 3 August 2001
Online at stacks.iop.org/PSST/10/502

Abstract
The ionized metal physical vapour deposition (IMPVD) process is being developed to produce metal seed layers and diffusion barriers in deep contacts and vias for microelectronics fabrication. An IMPVD reactor is typically an antenna excited system where transmission line effects may produce asymmetric ion fluxes to the target and hence an asymmetric distribution of sputtered metal species in the reactor. A possible result is a non-uniform metal deposition on the wafer. In this paper, a three-dimensional model for an IMPVD reactor is employed to examine the consequences of asymmetric excitation and irregular sputter tracks on species' densities and fluxes. It was found that for typical conditions for Al IMPVD severe asymmetries in electron temperature and electron density profiles produced by a poorly optimized antenna are not reflected in the metal fluxes to the substrate. The metal species have improved symmetry due to charge exchange of the buffer gas ions to the metal and the higher mobility of the metal ions relative to the buffer gas ions. The symmetry and uniformity of the metal species above the wafer significantly improve when increasing the aspect ratio of the plasma region or increasing the pressure due to there being more diffusional transport. However, this improvement is accompanied by a decrease in the magnitude of metal fluxes to the wafer. Irregular sputter tracks combined with rotation of the target were also investigated.

1. Introduction

The ionized metal physical vapour deposition (IMPVD) process is rapidly becoming the semiconductor industry's preferred method of filling deep contacts and vias with metal seed layers and diffusion barriers [1–3]. In an IMPVD reactor, the sputtered metal atoms from the magnetron target are ionized by a secondary plasma before arriving at the substrate. The secondary source is typically an inductively coupled plasma (ICP). Uniformity, directionality, and deposition rate are important process parameters in IMPVD. However, azimuthal asymmetries in these parameters can arise in an IMPVD process due to the antenna design, reactor geometry, gas supply or sputter track design [4–7]. In particular, improper antenna design can lead to azimuthal variations in coil current, which in turn produces an azimuthally asymmetric inductively coupled electric field, electron density and ion densities. The imprint of these densities may persist to the incident metal fluxes to the substrate.

The consequences of antenna design have been investigated experimentally and numerically for ICP etching

[3] Present address: Novellus Systems, 4000 North First Street, San Jose, CA 95134, USA
[4] Author to whom correspondence should be addressed.

reactors [4, 5]. Kushner *et al* [4] performed a three-dimensional simulation of an ICP etching reactor at 5 mTorr Cl_2 and 250 W ICP power. Considerable asymmetries in electron density, temperature and ion flux to the substrate were shown to result from transmission line effects in the antenna. For a reactor with a one-turn coil, the predicted and experimentally measured azimuthal variations in electron density 1 cm above the substrate edge reached 40% (as determined by (maximum − minimum)/average) and the maximum ion flux to the substrate was off-centre. These asymmetries diminished with the use of a five-turn coil. Khater and Overzet [5] designed an ICP source consisting of a three-dimensional coil having two layers of full and semicircular loops with the radio frequency (rf) current generally flowing in opposite directions. The electric fields had improved azimuthal asymmetry compared with a simple planar coil. For an ICP power of 1 kW, the azimuthal variation of the electric field of the improved source was up to 9% at a radius of 7 cm and 1 cm below the dielectric window. The azimuthal variation was 16% for the planar coil. At 3 mTorr Cl_2 and 900 W ICP power, the non-uniformity in polysilicon etching for the improved source was 5%, compared to 7.5% for the planar coil.

IMPVD systems differ from typical etching systems in that the sputtered metal atoms typically have lower ionization potentials than the buffer gas atoms and the buffer gas density is usually large compared to the metal atom density. The mobility of the buffer gas ions is therefore constrained by both rapid symmetric charge exchange with other buffer gas atoms and by non-symmetric charge exchange with the metal atoms. On the other hand the mobility of the metal ions is large in comparison. The metal ions have the lowest ionization potential in the system, and so will not charge exchange with other species. The rate of symmetric charge exchange is low among metal species because of the comparatively low density of metal atoms.

IMPVD systems also differ from etching systems or conventional PVD systems in that there is the potential for undesirable feed back. Should, for example, asymmetric excitation by the antenna produce asymmetric ionization, the resulting asymmetric ion fluxes to the target can produce asymmetric metal sputtering. The asymmetric metal sputtering can then feed back, producing more metal atoms that are easily ionized. This can result in irregular target erosion and an asymmetric deposition profile [7]. In this paper, we will investigate these processes by considering the consequences of asymmetric excitation and irregular sputter tracks in the resulting species asymmetries in an IMPVD reactor. It was found that the asymmetry for sputtered metal species is significantly improved by the diffusion of the more mobile metal ions. Increasing the aspect ratio of the plasma region and increasing pressure improved the symmetry and uniformity of the metal species above the wafer but reduced the magnitude of metal fluxes to the wafer. Irregular sputter tracks act as an asymmetric sputter source and directly contribute to asymmetries in metal species. The model employed in this study is described in section 2. The results of this study are described in section 3. Concluding remarks are given in section 4.

2. Description of the model

The computational platform used in this study is the three-dimensional Hybrid Plasma Equipment Model (HPEM-3D) [4, 6]. HPEM-3D is a modular simulation which iteratively achieves a quasi-steady-state solution. The modules used here are the Electromagnetics Module (EMM), the Electron Energy Transport Module (EETM) and the Fluid Kinetics Module (FKM). Inductively coupled electric and magnetic fields are computed in EMM. These fields are then used in EETM to solve for the average electron energy as a function of position. The electron energies are used to compute source rates for electron impact processes and electron transport coefficients. These rates and coefficients are then used in the FKM where continuity and momentum equations are solved for all heavy particles (neutrals and ions) and Poisson's equation is solved for plasma potential throughout the reactor. The sputter transport algorithms are also included in the FKM. Densities and electric fields are then transferred to the EMM and EETM, and the process is repeated until a converged solution is obtained. The coordinate system is cylindrical (r, θ, z).

Briefly, the governing equations are as follows. In the EMM, the wave equation is solved for electric field $\boldsymbol{E}$ in the frequency domain:

$$\nabla \cdot \frac{1}{\mu} \nabla \boldsymbol{E} = \frac{\partial^2(\varepsilon_0 \boldsymbol{E})}{\partial t^2} + \frac{\partial(\overline{\overline{\sigma}}\boldsymbol{E} + \boldsymbol{J}_0)}{\partial t} \tag{1}$$

where $\overline{\overline{\sigma}}$ is the tensor conductivity of the plasma [8]. $\boldsymbol{J}_0$ represents externally driven coil currents obtained from a transmission line model for the antenna whose details are discussed in [4]. The antenna elements are one-to-one mapped onto locations on the transmission line. The resulting transmission line currents are then mapped back onto the antenna structure.

The static magnetic field generated by permanent magnets is computed by placing small current loops with current density $\boldsymbol{j}_e$ throughout the materials designated as magnets. The direction and magnitude of the current loops are adjusted to provide the desired static magnetic field profile. The current loops provide source terms for magnetic vector potential $\boldsymbol{A}$, whose curl is the static magnetic field $\boldsymbol{B}_s$,

$$\nabla \times \frac{1}{\mu} \nabla \times \boldsymbol{A} = \boldsymbol{j}_e \qquad \boldsymbol{B}_s = \nabla \times \boldsymbol{A}. \tag{2}$$

In the EETM, the electron energy equation is solved for electron temperature T_e in the steady state,

$$\frac{\partial}{\partial t}\left(\frac{3}{2} n_e k T_e\right) = \overline{\overline{\sigma}}\boldsymbol{E} \cdot \boldsymbol{E} + (\boldsymbol{j} \cdot \boldsymbol{E}_s)_{dc} - \nabla \cdot \left(\frac{5}{2} k T_e \overline{\varphi}_e - \overline{\overline{\lambda}} \nabla T_e\right) - n_e \sum_i k_i N_i \delta\varepsilon_i \tag{3}$$

where $\overline{\overline{\sigma}}\boldsymbol{E} \cdot \boldsymbol{E}$ is Joule heating by the inductively coupled fields and $(\boldsymbol{j} \cdot \boldsymbol{E}_s)_{dc}$ is the dc Joule heating by conduction currents from the electrostatic fields, $\overline{\varphi}_e$ is the electron flux, $\overline{\overline{\lambda}}$ is the tensor electron thermal conductivity, k_i is the rate coefficient for collisions between electrons and heavy species i of density N_i and $\delta\varepsilon_i$ is the energy loss by an electron per collision.

In the FKM, the continuity equation is solved for electrons assuming drift diffusion transport. Continuity and momentum

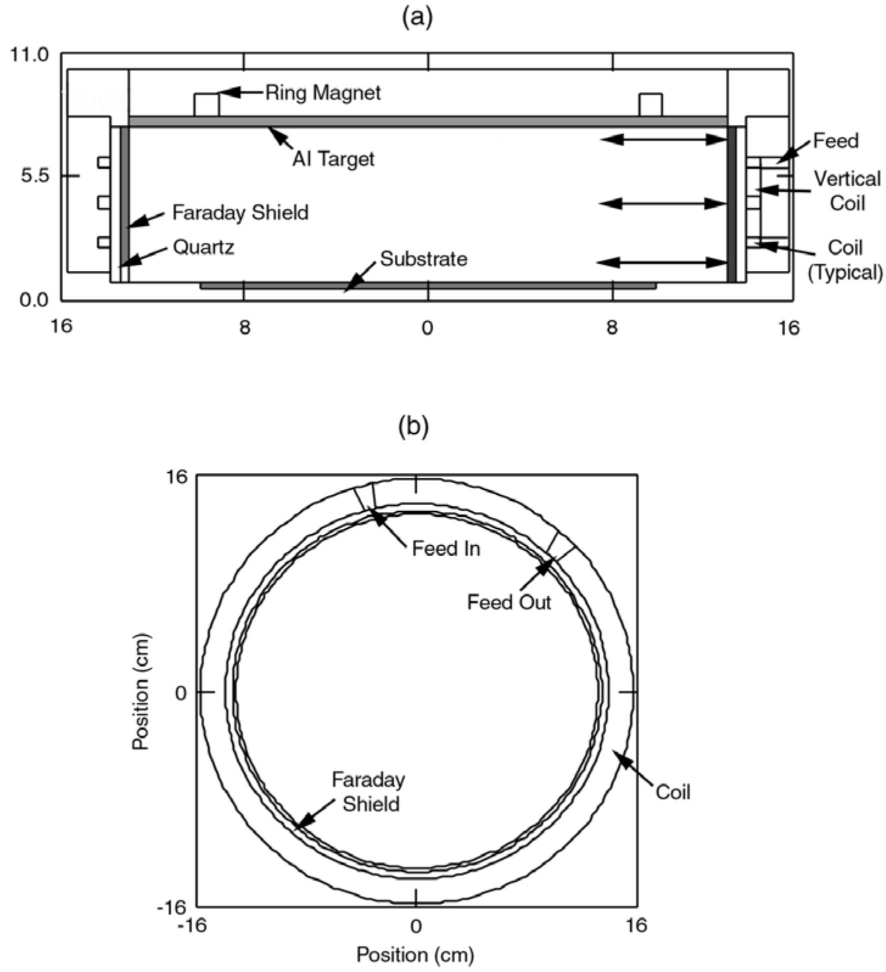

Figure 1. A schematic diagram of the IMPVD reactor used for this study: (a) side view, (b) top view. The reactor has a Faraday shield and a three-turn external coil. The azimuths of the vertical feeds are shown in the top view. The axial location of the r–θ slices (below target, mid-reactor, above wafer) are shown in the side view.

equations are employed for heavy particles. The heavy species energy equations are not solved so isothermal conditions are assumed throughout the reactor. The governing equations are

$$\frac{\partial n_e}{\partial t} = -\nabla \cdot (q_e n_e \overline{\overline{\mu}}_e \cdot \boldsymbol{E}_s - \overline{\overline{D}}_e \cdot \nabla n_e) + S_e \quad (4)$$

$$\frac{\partial N_i}{\partial t} = -\nabla \cdot (\boldsymbol{v}_i N_i) + S_i \quad (5)$$

$$\frac{\partial (N_i \boldsymbol{v}_i)}{\partial t} = \frac{q_i(\boldsymbol{E}_s + \boldsymbol{v}_i \times \boldsymbol{B}_s)}{m_i} - \nabla P_i - \nabla \cdot (N_i \boldsymbol{v}_i \boldsymbol{v}_i) - \nabla \cdot \overline{\overline{\tau}}_i + \sum_j N_i N_j k_{ij} (\boldsymbol{v}_j - \boldsymbol{v}_i) \quad (6)$$

where n_e, q and S_e are electron density, electric charge and electron source term; $\overline{\overline{D}}_e$ and $\overline{\overline{\mu}}_e$ are the diffusion and mobility coefficient tensors due to static magnetic field $\boldsymbol{B}_s$; N_i, $\boldsymbol{v}_i$ and P_i are the density, velocity and thermodynamic pressure of heavy species i, $\overline{\overline{\tau}}_i$ is the viscosity tensor; S_i is the source of species i due to all collisions; and k_{ij} is the rate coefficient for momentum transfer collisions between heavy species i and j. Slip boundary conditions are employed for the momentum equation using the method described by Thompson [9]. (Slip boundary conditions allow there to be a non-zero transverse gas velocity at surfaces to account for long-mean-free-path transport which occurs at low pressures.) The electrostatic field $\boldsymbol{E}_s$ is obtained from solution of Poisson's equation for the electrostatic potential Φ in the FKM,

$$-\nabla \cdot \varepsilon \nabla \Phi(t + \Delta t) = \rho(t) + \Delta t \sum_i q_i(-\nabla \cdot \overline{\phi}_i(t) + S_i) + \Delta t q_e(-\nabla \cdot (q_e n_e(t) \overline{\overline{\mu}}_e \cdot \nabla \Phi(t + \Delta t) - \overline{\overline{D}}_e \cdot \nabla n_e(t)) + S_e) \quad (7)$$

where ρ is the charge density and ε is the permittivity. The terms on the right-hand side are the implicit correction for updating $\Phi(t)$ for use at time $t + \Delta t$. The first term is for charge change due to ion transport and the second term is for electron transport.

Algorithms were also incorporated into the FKM to simulate sputtered atom transport. The kinetic energy of the emitted atoms from the target is given by Thompson's theory of atomic collision cascades [10] for incident ions of moderate energy (hundreds of electronvolts). The Thompson distribution can be approximated by a cascade distribution. However in the threshold energy regime (less than 50 eV), the validity of the Thompson distribution is questionable. The

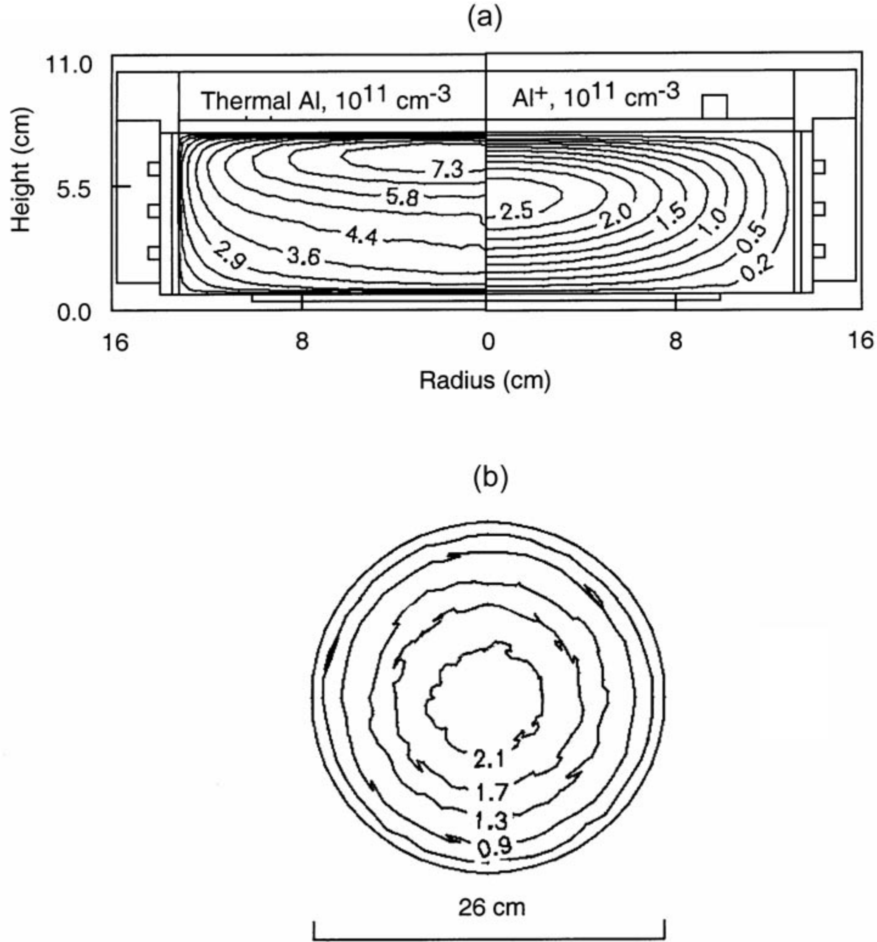

Figure 2. Al species densities ($\times 10^{11}$ cm^{-3}) and Al flux to wafer at 10 mTorr and $h/r = 0.5$ for symmetric excitation. (a) Thermal Al and Al^+ densities in the r–z plane, and (b) total Al flux to wafer (10^{16} cm^{-2} s^{-1}). Except for numerical noise, the fluxes and densities are azimuthally symmetric.

cascade distribution [10–12] is

$$F(E) \propto \frac{U_S E}{(U_S + E)^3} \tag{8}$$

where E is the kinetic energy of the sputtered atom. The Thompson distribution peaks at half the surface binding energy U_s (3.4 eV for an Al target). Due to the high-energy tail of the distribution, the average energy of the sputtered Al atoms is generally several electronvolts. Under typical operating conditions, the incoming ion energy is approximately equal to the dc bias applied to the target.

The sputtered atoms are represented by pseudoparticles. Each computational pseudoparticle carries a 'weighting' that is used to determine its contributions to the thermalized atom density when it slows as a result of collisions with bulk gas atoms. The weighting of sputtered atoms originating at target location i and slowing to thermal speed in volume element j is

$$W_{ij} = \frac{Y(E_i)\varphi(\vec{r}_i)A(\vec{r}_i)}{N(\vec{r}_i)V(\vec{r}_j)} \tag{9}$$

where Y is the sputter yield of the target bombarded by ions with energy E_i, φ is the flux of ions and fast neutrals to the target at $\vec{r}_i$ (fast neutrals and ions of the same energy are considered equivalent with respect to sputtering), N is the number of Monte Carlo particles released from that location, $A(\vec{r}_i)$ is the surface area of the computational cell on the target at $\vec{r}_i$ and $V(\vec{r}_j)$ is the volume of the computational cell at $\vec{r}_j$ where the sputtered atom is thermalized.

The sputtered atoms are emitted at an angle with a cosine distribution from the target surface. Monte Carlo techniques are then used to follow the trajectories of the emitted atoms. The mean free path of the sputtered atom is determined using null collision techniques [12] to account for the composition variation of the background gas due to the slowing of the sputtered atoms. Collisions with gas atoms exchange only translational energy (electronic energy exchange is ignored). The sputtered atoms that slow down to thermal speeds are recorded in a source term for the continuity equation,

$$\frac{\mathrm{d}n(\vec{r}_j)}{\mathrm{d}t} = \sum_i W_{ij} \tag{10}$$

where n is the density of the sputtered metal atoms, and the sum for its derivative at location j is over all target locations i. The non-thermal Al neutrals incident on the substrate are recorded in source terms that are used to compute fluxes to the substrate.

The Ar/Al reaction mechanism has been previously described in detail [14]. The majority of the processes

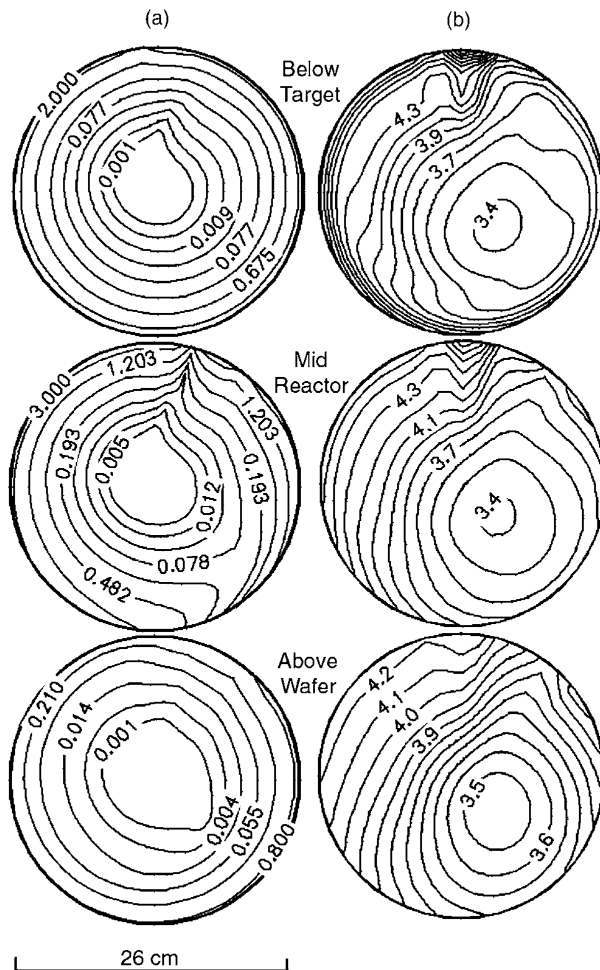

Figure 3. Azimuthal asymmetries in (a) magnitude of the inductively coupled electric field (V cm^{-1}) and (b) electron temperature at three r–θ planes at 10 mTorr and $h/r = 0.5$ for asymmetric excitation. The electric field is asymmetric and larger in the upper-left quadrant and the resulting asymmetry electron temperature is consistent with the electric field.

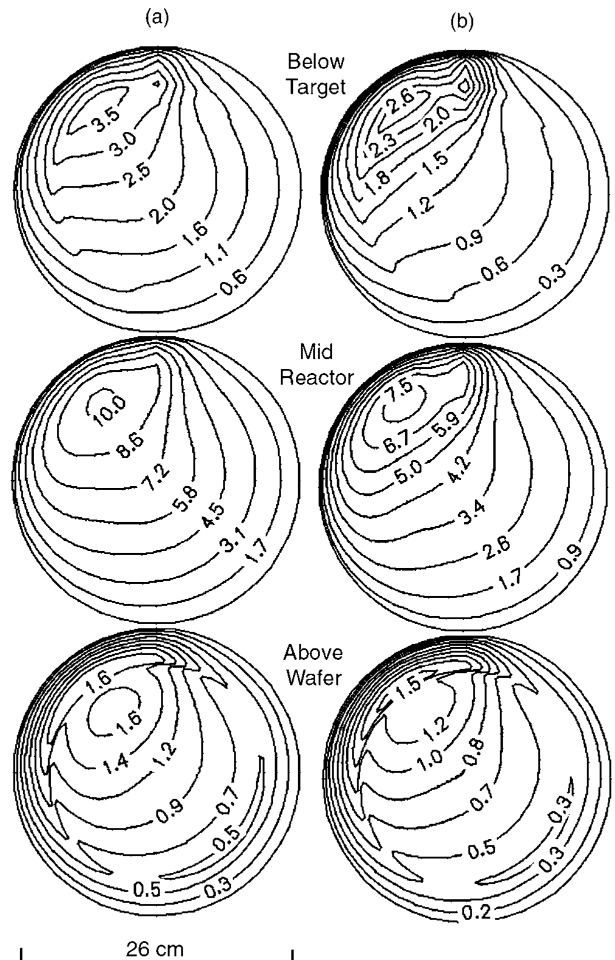

Figure 4. Densities ($\times 10^{11}$ cm^{-3}) of (a) electrons and (b) Ar^+ at three r–θ planes at 10 mTorr and $h/r = 0.5$ for asymmetric excitation. The electron and Ar^+ densities peak in the upper-left quadrant, consistent with the electric field.

belong to either electron-impact reactions or charge-exchange reactions. The electron–Ar chemistry includes electron impact excitation of Ar from the ground state to the excited states 4s and 4p, which are lumped into a single excited state, and electron impact ionization (from the Ar ground state and the excited state). The electron–Al chemistry includes electron impact excitation of Al from the ground state to the excited states 4s, 3p, 3d and 4p, super-elastic collision to de-excite Al^* to the ground state and electron impact ionization (from the Al ground state and the excited states). The radiative relaxation of Al^* to the ground state is rapid and Al^* is quenched by collisions with Al, Al^* and Ar. The Ar^* reacts with Ar^* to produce Ar^+, and with Al or Al^* to produce Al^+. Charge-exchange reactions of Ar^+ with Ar and Al play an important role in generating fast neutral fluxes to the target and in ionizing Al atoms before they reach the substrate. The reaction rates for charge exchange are large, approximately 10^{-9} $cm^3\,s^{-1}$. The charge-exchange reactions include resonant exchange among the Ar species and non-resonant exchange between Ar (ionization potential 15.8 eV) and Al (6.0 eV) species.

3. Effects of asymmetric excitation and irregular sputter track

A schematic diagram of the cylindrical IMPVD reactor employed in this study is shown in figure 1. The reactor utilizes a Faraday shield [15] with external coils. This configuration is based on a commercial reactor [16] (Tokyo Electron-Arizona webpage http://www.telusa.com). With external coils, sputtering and capacitive coupling from the coils are eliminated. A ring magnet is located on top of the Al target. The antenna consists of a three-turn solenoid with vertical segments linking each turn. The excitation current enters from the feed on the top-turn coil and exits from the feed on the bottom-turn coil. The termination impedance of the coil is 100 pF. The substrate is 10 cm in radius and the target-to-substrate distance is 6.5 cm. The internal radius of the plasma region is 13 cm and so the aspect ratio (height/radius or h/r) is 0.5. The base case conditions are 600 W ICP power at 13.56 MHz, 10 mTorr Ar gas, -100 V dc bias on the aluminium target and -20 V bias on the substrate. The static magnetic field is 200 G below the ring magnet. The neutral species temperature is assumed to be 375 K and the ion species temperature is $\approx$0.1 eV, typical values for the bulk

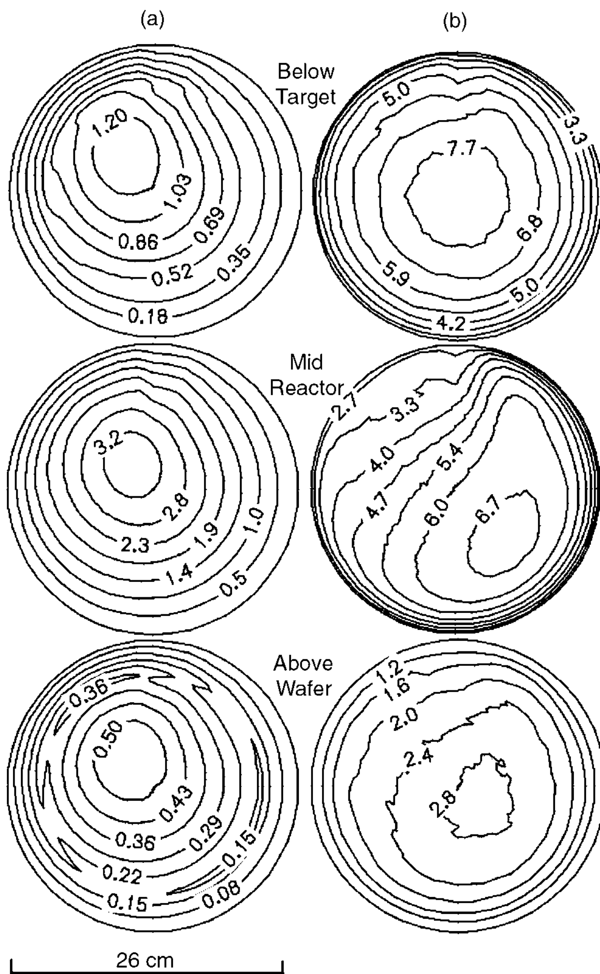

Figure 5. Al species densities ($\times 10^{11}$ cm^{-3}) at three r–θ planes at 10 mTorr and $h/r = 0.5$ for asymmetric excitation. (a) Al^+ and (b) thermal Al. The uniformity of Al^+ is better than that of the electrons and Ar^+ due to charge exchange and its higher mobility, while the less mobile Al atoms retain the asymmetry of the sputter source.

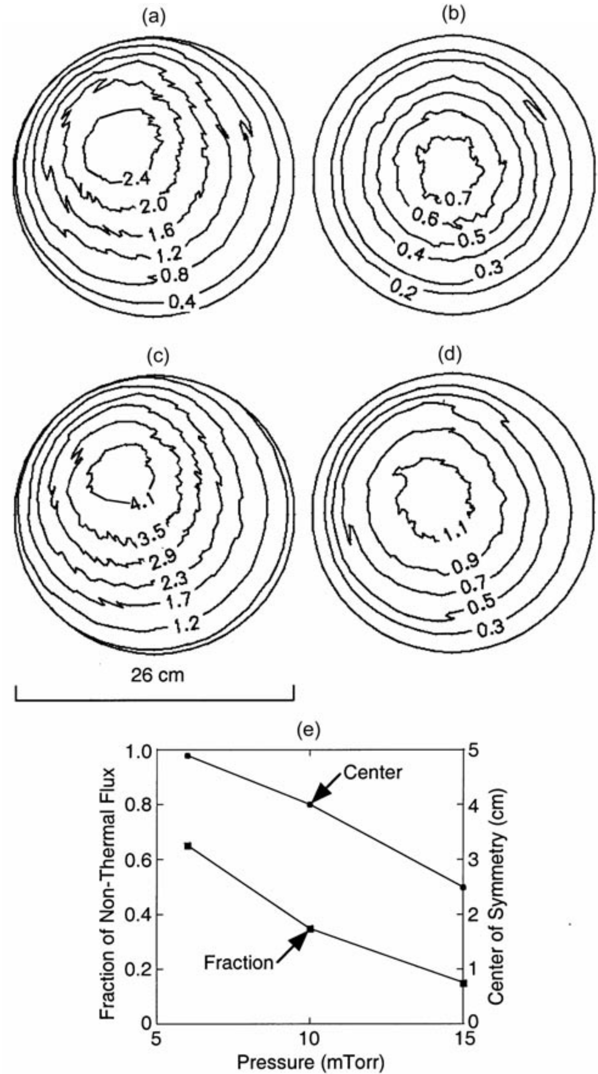

Figure 6. Total Al flux to the wafer for asymmetric excitation (10^{16} cm^{-2} s^{-1}) at (a) 10 mTorr, $h/r = 0.5$; (b) 10 mTorr, $h/r = 0.75$; (c) 6 mTorr, $h/r = 0.5$; (d) 15 mTorr, $h/r = 0.5$; and (e) the fraction of non-thermal Al flux to the substrate and centre of asymmetry as a function of pressure at $h/r = 0.5$. The fraction of non-thermal flux decreases and the asymmetry of the deposition improves with increasing pressure.

regions of inductively coupled plasmas [16]. In order to isolate the effects of electromagnetic and physical asymmetries, the gas temperature was held constant. Although the chosen temperature is somewhat lower than expected when compared to those predicted by two-dimensional models and measured in experiments, the important parameter in computing the scattering of sputtered species is the mean free path which is a function of gas density and only weakly dependent on the absolute temperature. One can therefore scale these results to other temperatures based on gas density or average mean free path. A constant sputter yield of 1.2 was used for the entire Al target. This yield is more realistic for a target bias of −300 to −400 V. A numerically more tractable −100 V was used here. Since the bias on the target is mostly consumed in the sheath, the potential in the bulk plasma is not significantly affected by the bias voltage. The plasma quantities were examined at three r–θ planes: below the target, at mid-reactor and above the wafer, as indicated in figure 1(a).

For comparison purposes, symmetric excitation was first applied to the antenna by forcing the conduction current through all antenna segments to be equal. Under symmetric excitation, the species in the reactor are essentially azimuthally symmetric. The thermal Al and Al^+ densities in a typical r–z plane, shown in figure 2(a), are on the order of 10^{11} cm^{-3}. (Species densities are given by the contour label multiplied by the scaling factor at the top of each figure. This labelling scheme is typical for all contour plots.) The Al density is a maximum below the target due to the proximity of the sputter source. The thermal Al density then decreases toward the wafer by both diffusion and ionization. The Al^+ density peaks farther below the target as the Al atoms need to travel some distance before ionization collisions occur and the plasma potential peaks near mid-reactor. Al^+ is somewhat depleted above the wafer by the negative bias. The total Al flux to the wafer, shown in figure 2(b), is symmetric except for some statistical noise due to the non-thermal Al flux from the target. (Note that the entire plane of the plasma (radius of 13 cm) is plotted, whereas the wafer radius is only 10 cm.) The total

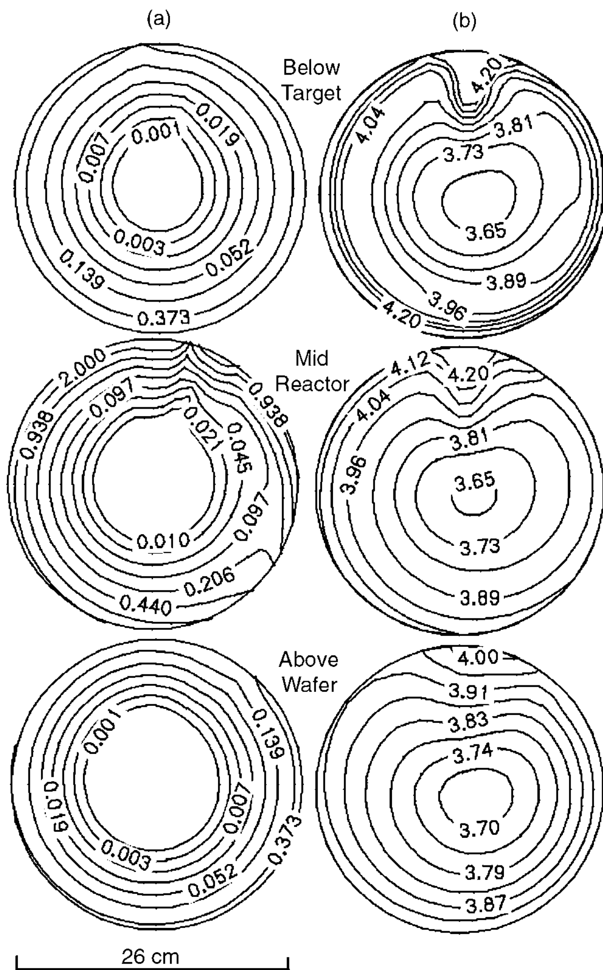

Figure 7. Azimuthal asymmetries of (a) the magnitude of the inductively coupled electric field (V cm^{-1}) and (b) the electron temperature at three r–θ planes at 10 mTorr and $h/r = 0.75$ for asymmetric excitation. The distribution of the electric field is similar to that for $h/r = 0.5$. The electron temperature is more symmetric and uniform than that for $h/r = 0.5$ due to the longer diffusion lengths.

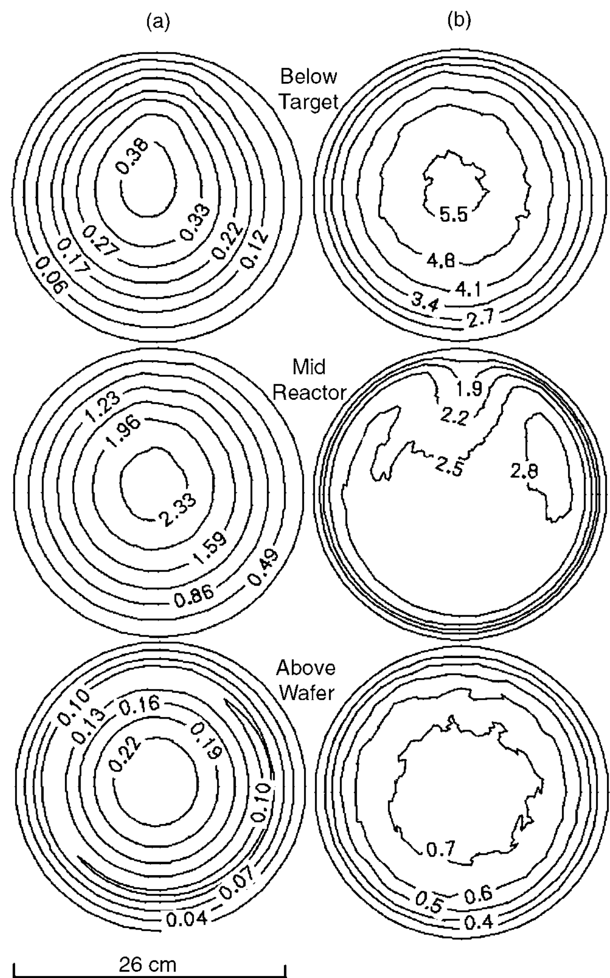

Figure 8. Al species densities ($\times10^{11}$ cm^{-3}) at three r–θ planes at 10 mTorr and $h/r = 0.75$ for asymmetric excitation. (a) Al^+ and (b) thermal Al. Both densities are more uniform and symmetric due to the longer diffusion lengths.

Al flux includes contributions from Al (both thermal and non-thermal), Al^+ and Al^*. The contribution from Al^* is at least one order of magnitude smaller than that from Al and Al^+ due to depletion by ionization and radiative relaxation before reaching the wafer. The ionization fraction of the Al flux to wafer is 40% near the centre and 30% near the periphery.

Asymmetric excitation was applied to the plasma while the rest of the operating conditions and geometry remained the same as those of the base case. This asymmetry resulted from transmission line effects which produced non-uniform conduction currents along the antenna. The magnitude of the inductively coupled electric field in the plasma is shown in figure 3(a). The electric field is fairly symmetric and uniform below the target except for minor asymmetries in the upper-mid portion. These minor asymmetries result from the vertical transverse of the antenna from one turn to the next. The electric field is maximum (of the order of 3 V cm^{-1}) on the edge of the plasma due to the solenoid coils and decays exponentially into the plasma with a skin depth of about 2 cm. The electric field amplitude is a maximum at mid-reactor height, due to the constructive interference of the electric fields generated from the three turns of the coil. The asymmetry of the electric field is also most severe at mid-reactor due to the non-uniform distribution of the current on the coil and due to the axial segments of the coil. Besides the sharp peaks in the mid-upper portion, the electric field is only 0.2–0.5 V cm^{-1} at the lower-right edge of the plasma, significantly lower than the 3 V cm^{-1} at the upper-left edge of the plasma. Such asymmetries are caused by the non-uniform conduction current along the length of the coil. The symmetry above the wafer is somewhat better than that at mid-reactor, although the field at the lower-right edge is larger than that at the upper-left edge.

The resulting electron temperatures are shown in figure 3(b). The electron temperatures are high throughout the reactor, from 3.4 to 4.7 eV, due to the large thermal conductivity of the plasma. The electron temperatures are minimum in the plasma at the lower-right edge, increasing toward the upper-left and lower-right edges. This pattern of electron temperature is consistent with the larger electric fields at mid-reactor at the upper-left edge due to the coil asymmetry. The resulting electron and Ar^+ densities are shown in figure 4. The electron density has a maximum of $\approx10^{12}$ cm^{-3} at the upper-left edge

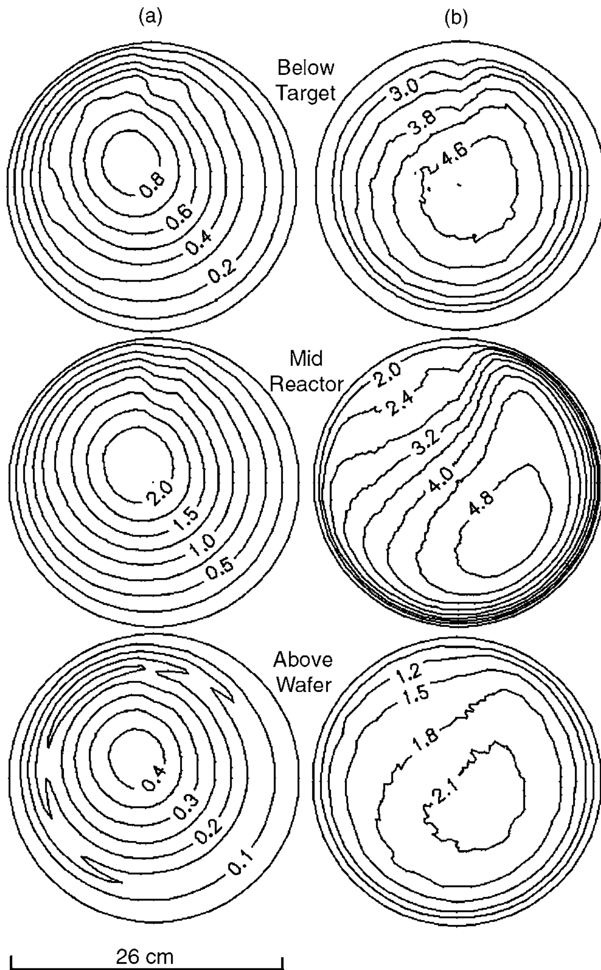

Figure 9. Al species densities ($\times 10^{11}$ cm^{-3}) at three r–θ planes at 6 mTorr and $h/r = 0.5$ for asymmetric excitation. (a) Al^+ and (b) thermal Al. Both densities decrease with decreasing pressure.

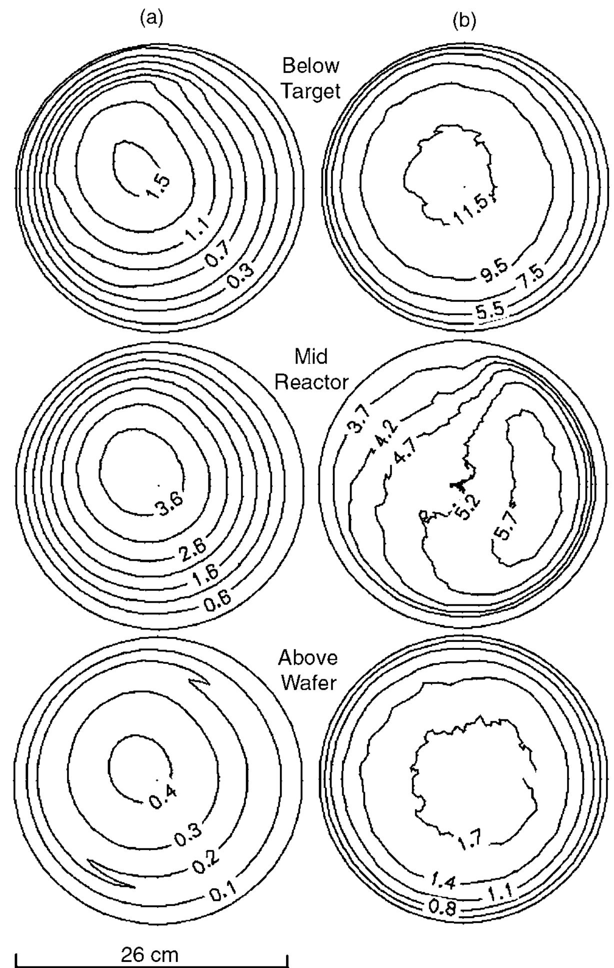

Figure 10. Al species densities ($\times 10^{11}$ cm^{-3}) at three r–θ planes at 15 mTorr and $h/r = 0.5$ for asymmetric excitation. (a) Al^+ and (b) thermal Al. Thermal Al density increases with increasing pressure, while the Al^+ density above the wafer decreases.

where the electric field and the electron temperature are the largest. The Ar^+ density is similar to the electron density as Ar^+ is the dominant ion. The significant azimuthal asymmetry above the wafer, which mirrors the outline of the substrate, results from the current collected by the biased substrate. The Al^+ density is shown in figure 5(a). The maximum Al^+ density is $\approx 3 \times 10^{11}$ cm^{-3}, approximately 40% of that of Ar^+. The Al^+ is generally more uniform than the electrons and Ar^+. Al, having a lower ionization potential than Ar, can be ionized by a larger fraction of the electron energy distribution over a larger portion of the reactor. Ar, with the larger ionization potential, is preferentially ionized at the upper-left edge where the electron temperature is highest. Al atoms also undergo charge-exchange reactions with Ar^+ to form the more mobile Al^+. The Al^+ then diffuses toward the centre of the reactor under the influence of the ambipolar electric fields, thereby mitigating the asymmetry due to its ionization sources. Above the wafer the Al^+ ions, on the order of 10^{10} cm^{-3}, are depleted by the substrate bias of -20 V.

The thermal Al density shown in figure 5(b) is fairly symmetric below the target in spite of the asymmetric Ar^+ density and hence sputter source. The thermal Al density is asymmetric at mid-reactor in mirror image to the ion and electron densities. This trend is due to depletion of the neutral Al by electron impact ionization, charge-exchange and Penning processes in the upper left where T_e is the largest. The Al atoms, being less mobile than the Al^+ ions, retain the imprint of this asymmetry of the sputter source to a greater degree than the Al^+ ions.

The total Al flux to wafer (sum of neutral Al and Al^+) shown in figure 6(a) has an asymmetry similar to that of the Al^+ density above the wafer, shown in figure 5(a). The ionization fraction of the Al flux ranges from 40% near the centre to 25% near the upper-left edge of the plasma, and 30% for the rest. Although the thermal Al and Al^+ have similar densities, the Al^+ ions arrive at the sheath edge with a Bohm velocity which is about seven times the random thermal velocity of the Al atoms. This larger velocity, and hence larger flux, dominates over that of the thermal Al. At 10 mTorr and 375 K, the mean free path of the Al atoms in Ar is about 1.5 cm. A significant number of non-thermal Al atoms produced at the target survive to reach the substrate. These non-thermal atoms account for about 35% of the total Al flux. This non-thermal component of the Al flux tends to reinforce the asymmetry of the Al^+ flux since the non-thermal flux originates from asymmetric sputtering of the

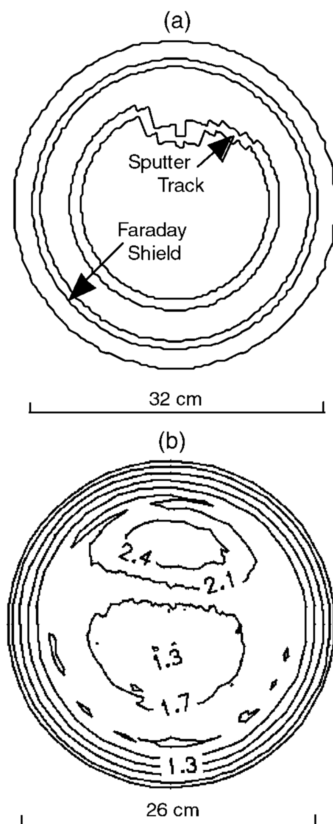

Figure 11. Sputter track and total Al flux to the wafer. (a) Schematic diagram of the irregular heart-shaped sputter track and (b) total Al flux to wafer ($\times 10^{16}$ cm^{-2} s^{-1}) for symmetric excitation at 10 mTorr, $h/r = 0.5$. The asymmetry in the Al flux mirrors that of the sputter track.

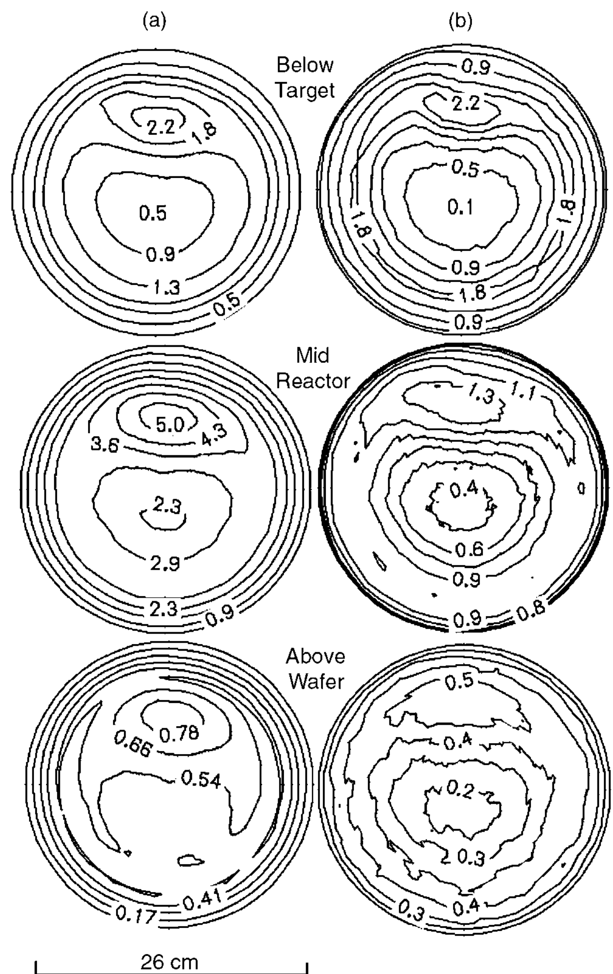

Figure 12. Al species densities at three r–θ planes at 10 mTorr and $h/r = 0.5$ for symmetric excitation and an irregular sputter track. (a) Al^+ ($\times 10^{10}$ cm^{-3}) and (b) thermal Al ($\times 10^{11}$ cm^{-3}). Both densities are asymmetric throughout the reactor.

target. The thermal Al neutrals, being more uniform than the Al^+ ions and non-thermal Al neutrals, alleviate some of the non-uniformity in the total Al flux.

The consequences of the reactor aspect ratio on the incident metal flux to the substrate was investigated by increasing the target-to-wafer distance from 6.5 to 9.75 cm, a 50% increase, which increased the aspect ratio of plasma region from 0.5 to 0.75. The distribution of the inductively coupled electric field for an aspect ratio of 0.75 (shown in figure 7(a)) is similar to that for the smaller aspect ratio (shown in figure 3(a)). The magnitude of the electric field for the larger aspect ratio is less by half below the target and above wafer. The smaller magnitude is due to the exponential decay of the electric field in the plasma and the further distance from the coils.

The electron temperature is more symmetric and uniform in the larger reactor, as shown in figure 7(b). T_e ranges from 3.5 to 4.5 eV throughout the reactor. The larger aspect ratio provides more volume for thermalization and transport, and the diffusion tends to homogenize the electron temperature in the reactor. This longer diffusion distance is also the reason that the Al^+ density is more symmetric and the thermal Al density is more uniform for the large aspect ratio, as shown in figure 8. With the exception of the Monte Carlo generated noise, the thermal Al density above the wafer is essentially symmetric. However, the uniformity and symmetry at the large aspect ratio are achieved at the expense of the magnitude of the incident metal flux to the substrate. The thermal Al density above the wafer for the larger aspect ratio is only one-fourth to one-third that for the smaller aspect ratio. The Al^+ density above the wafer is only one-third to a half that of the smaller aspect ratio. The more symmetric total Al flux to wafer, shown in figure 6(b), is also only about one-third to one-half that of the smaller aspect ratio, as shown in figure 6(a). The non-thermal Al flux now accounts for only 12% of the total, a consequence of the larger distance from the target and increased opportunity for thermalizing collisions.

The Al species densities for lower (6 mTorr) and higher (15 mTorr) pressures are shown in figures 9 and 10. For both pressures the basic patterns of asymmetries for both thermal Al and Al^+ are similar to those at 10 mTorr. The degree of asymmetry, as indicated by the gradients in these quantities, worsens in going to lower pressure. At the lower pressure, the imprint of the asymmetric sputtering pattern has insufficient opportunity to be dissipated by collisions. At higher pressure, the thermal Al densities increase with pressure throughout the reactor (from (2.0–4.8) $\times$ 10^{11} cm^{-3} at mid plane for 6 mTorr to (3.7–5.7) $\times$ 10^{11} cm^{-3} at 15 mTorr) due to this increasing

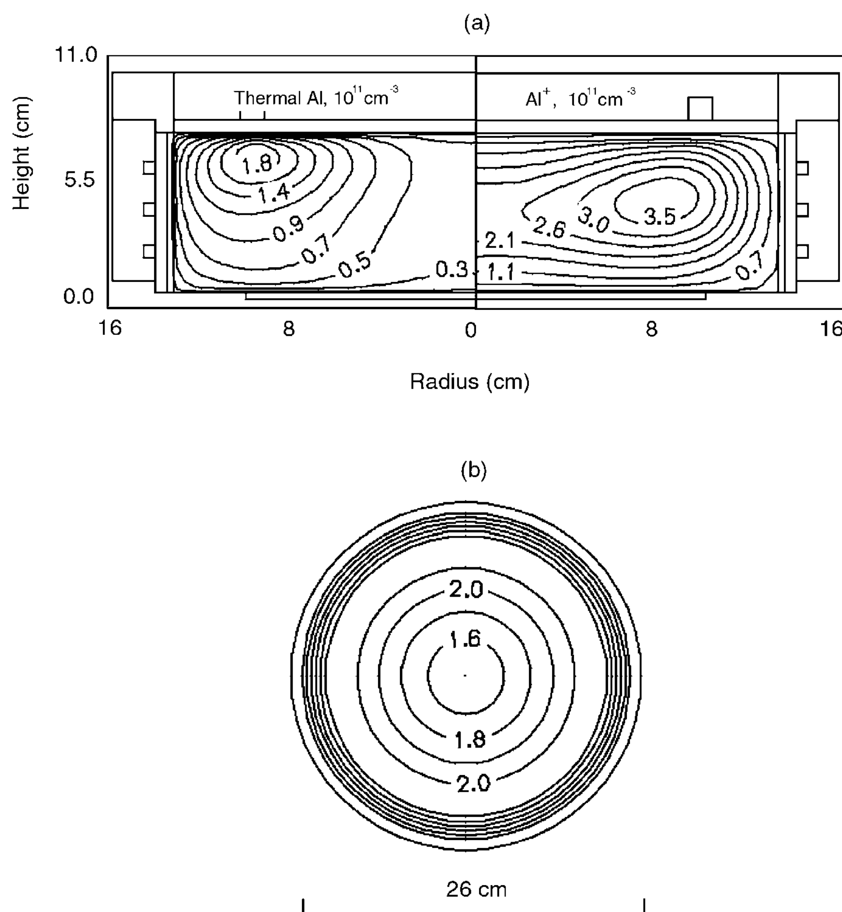

Figure 13. Al species densities and flux at 10 mTorr and $h/r = 0.5$ for symmetric excitation and a rotating irregular sputter track. (a) Thermal Al and Al^+ and (b) total Al flux to the wafer ($\times 10^{15}$ cm^{-2} s^{-1}). The Al density and Al flux distributions are heavily influenced by the sputter track, while the more mobile Al^+ ions peak mid-way between the target and the wafer.

frequency of collisions and thermalization of the sputtered Al atoms. Al^+ densities also generally increase with pressure.

The total Al fluxes to the substrate for 6 and 15 mTorr are shown in figures 6(c) and 6(d), respectively. The total Al flux to the wafer decreases with pressure due to the increased rate of scattering of sputtered Al atoms and the diminishing survival of the non-thermal Al flux to the substrate. The non-thermal Al flux accounts for 65% of the total at 6 mTorr, but only 15% as the pressure is increased to 15 mTorr, as shown in figure 6(e). The consequences of pressure on the symmetry of the Al flux to the substrate are also shown in figure 6(e). The radius of the central peak in the Al flux, R_0, is used as a measure of the asymmetry. R_0 decreases from 4.9 cm at 6 mTorr to 2.5 cm at 15 mTorr, indicating an improvement in symmetry with pressure. This improvement results from both a decreased contribution of the non-thermal flux and increased diffusion of the thermalized atoms.

The sputter track used for the cases thus far was symmetric. Conventional magnetrons often use asymmetric sputter tracks with the intent of maintaining process parameters as the target erodes with use. The magnets behind the target are rotated in order to symmetrize the flux to the substrate. Although non-rotated, asymmetric sputter tracks are rarely, if ever, used in commercial PVD reactors, it is nevertheless interesting to investigate the intrinsic asymmetries produced by the unrotated target. In this regard, the heart-shaped sputter track pattern shown in figure 11(a) was used in the model, a pattern similar to those used in commercial magnetrons [7]. The remainder of the reactor geometry and operating conditions are the same as those for the base case. To isolate the effect of the irregular sputter track, symmetric excitation was applied to the antenna. The resulting thermal Al and Al^+ densities are shown in figure 12 for an unrotated sputter track. For both species, the maximum for each plane occurs below the inverted part of the sputter track. The minimum for each plane occurs near the centre of the reactor, due to the lack of sputter source at that location. These asymmetries result in the asymmetric flux to the substrate shown in figure 11(b). The maximum Al flux occurs beneath the inverted track.

Because of these asymmetries in the metal flux caused by the irregular track, the magnets are usually rotated during the operation of a commercial magnetron tool. This mode of operation was modelled by azimuthally averaging the densities and species of the irregular-track case. The resulting thermal Al and Al^+ densities are shown in figure 13(a). The thermal Al density is a maximum below the sputter track and the Al^+ density is maximum further below the sputter track near the centre line due to the higher mobility of Al^+ in the ambipolar electric fields. The total Al flux to wafer shown in figure 13(b) has a maximum directly below the sputter

track and decreasing magnitude radially inward and outward. These results appear more azimuthally symmetric than the non-rotated, symmetrically excited case (figure 2). This is an artifact of the smoothing of Monte Carlo generated noise during the averaging process. Although appearing radially less uniform than the non-rotated case, this is not a general trend as the details of the radial uniformity critically depend on the details of the design of the sputter track

4. Concluding remarks

A three-dimensional model was used to investigate species asymmetries which may result from transmission line effects in the antenna and irregular sputter tracks in Al IMPVD. The asymmetric inductively coupled electric field produced by transmission line effects causes the electron temperature, and subsequently the electron and major ion densities, to be asymmetric. However, the uniformity of the metal ions is more symmetric as these species, by virtue of their low ionization potential, are both more mobile and produced over a broader spatial extent of the reactor. As the aspect ratio is increased from 0.5 to 0.75, asymmetries in the electric field and electron temperature are significantly mitigated. Consequently, the metal species become more symmetric above the wafer at the cost of decreasing the metal flux to the substrate by more than 50%. As the pressure increases, the Al flux to the substrate becomes more symmetric although the magnitude of the Al flux decreases. Irregular sputter tracks directly contribute to asymmetries in metal species and deposition flux by acting as an asymmetric source for the sputtered metal atoms. Rotation of the target is necessary to achieve azimuthal symmetry.

Acknowledgments

This work was funded by Semiconductor Research Corporation, National Science Foundation (CTS99-74962), DARPA/AFOSR, Applied Materials Inc. and Tokyo Electron-Arizona.

References

[1] Rossnagel S M 1996 *Semicond. Int.* **21** 99
[2] Hopwood J 1998 *Phys. Plasmas* **5** 1624
[3] Ryu C, Lee H, Kwon K W, Loke A L S and Wong S S 1999 *Solid State Technol.* **42** 53
[4] Kushner M J, Collison W Z, Grapperhaus M J, Holland J P and Barnes M J 1996 *J. Appl. Phys.* **80** 1337
[5] Khater M H and Overzet L J 2000 *Plasma Sources Sci. Technol.* **9** 545
[6] Kushner M J 1997 *J. Appl. Phys.* **82** 5312
[7] Rossnagel S M 1998 *J. Vac. Sci. Technol.* B **16** 2585
[8] Kinder R L and Kushner M K 2001 *J. Vac. Sci. Technol.* A **19** 76
[9] Thompson P A 1994 *Compressible Fluid Dynamics* (New York: McGraw-Hill) ch 2
[10] Thompson M W 1968 *Philos. Mag.* **18** 377
[11] Serikov V V and Nanbu K 1996 *J. Vac. Sci. Technol.* A **14** 3108
[12] Lieberman M A and Litchtenberg A J 1994 *Principles of Plasma Discharges and Material Processing* (New York: Wiley) p 523
[13] Bogaerts A, van Straaten M and Gijbels R 1995 *J. Appl. Phys.* **77** 1868
[14] Lu J and Kushner M J 2000 *J. Appl. Phys.* **87** 7198
[15] Bayer R, Lantsman A D and Seirmarco J A 1996 *US Patent Specification* 5569363
[16] Hebner G A 1996 *J. Appl. Phys.* **80** 2624